AAS 25-529

USING MOTION PRIMITIVES TO GENERATE INITIAL GUESSES FOR TRAJECTORIES TO SUN-EARTH L2

Natasha Bosanac*

This paper focuses on using a motion primitive approach to generate initial guesses for a planar spacecraft trajectory from an Earth-Moon L_1 Lyapunov orbit to a Sun-Earth L_2 Lyapunov orbit. Motion primitives are generated as fundamental building blocks of motion in each of the Earth-Moon and Sun-Earth circular restricted three-body problems. Sequences of these primitives are then generated by searching a motion primitive graph that captures their epoch-dependent sequential composability within and between dynamical models. These sequences are processed to extract geometrically distinct initial guesses for a planar transfer.

INTRODUCTION

Robotic servicing has the potential to increase the sustainability of space operations well beyond low Earth orbit. Mission concept development for prior and future large observatories operating in orbits around Sun-Earth L_2 have included discussions of the architecture and technologies required to render robotic servicing feasible [1–3]. In making this determination, key considerations that impact the trajectory of a robotic servicer spacecraft include, but are not limited to, 1) the holding location of a servicer spacecraft before transferring to the location of an observatory, 2) whether the observatory is serviced near Sun-Earth L_2, 3) the response time and maneuver requirements for the servicer spacecraft, and 4) whether a servicer could be reused, refueled, and/or transfer hardware components at a depot located in the Earth-Moon system. These outstanding questions benefit from analysis of the associated trajectory tradespace for a robotic servicer.

A wide variety of researchers within the astrodynamics community have used dynamical systems theory to study segments of the tradespace of trajectories between cislunar space and orbits near Sun-Earth L_1 or L_2. For instance, Farquhar, Muhonen, and Church presented complex trajectories for the International Sun-Earth Explorer 3 (ISEE-3) spacecraft from a Sun-Earth L_1 orbit to the Earth's geomagnetic tail [4]. Howell et al. generated multiple, geometrically distinct transfers from Earth-Moon libration point orbits to Sun-Earth L_2 orbits [5]. Folta and Webster generated transfers for a robotic servicer from Earth-Moon L_2 halo orbits and distant retrograde orbits to Sun-Earth L_2 [6]. Similarly, Ojeda Romero and Howell generated geometrically diverse transfers with impulsive maneuvers from a geosynchronous transfer orbits to periodic and quasi-periodic orbits near Sun-Earth L_1 and L_2 [7]. Pascarella et al. have also generated various trajectories with impulsive and continuous thrust maneuvers from an Earth-centered orbit to Sun-Earth L_2 [8]. These papers, and many more within the astrodynamics community, motivate continued development of procedures for generating complex trajectories across a diverse tradespace.

*Associate Professor, Colorado Center for Astrodynamics Research, Smead Department of Aerospace Engineering Sciences, University of Colorado Boulder, 3775 Discovery Drive, Boulder, CO 80303.

Recently, Smith and Bosanac introduced a motion primitive approach to trajectory design that was inspired by their use in robotics [9]. Motion primitives have been defined throughout the literature as fundamental building blocks of motion [10]. As a result, sequences of these primitives have supported constructing complex paths. Smith and Bosanac adapted this idea to define a motion primitive for spacecraft trajectories as an arc that summarizes the geometry of nearby arcs [9, 11]. Expanding upon their use in path-planning, Smith and Bosanac then constructed a motion primitive graph to generate initial guesses for spacecraft trajectories in the Earth-Moon system from sequences of these primitives [9]. Through their initial proof of concept, they demonstrated that motion primitives have the potential to support 1) rapid and automated trajectory design, and 2) efficient exploration of the trajectory trade space. Since this first proof of concept, Miceli and Bosanac have substantially built upon this procedure to improve the automation of the approach as well as the quality and diversity of the resulting initial guesses; this updated procedure is used as a foundation for this paper [12]. In addition, Gillespie, Miceli, and Bosanac have extended this idea to construct behavioral motion primitives that summarize natural and controlled arcs with a similar geometry while also encoding the associated maneuvering behaviors [13]. The improved procedure for generating the motion primitives, as presented in both of these papers, is used here.

This paper leverages a motion primitive approach to construct initial guesses for a planar spacecraft trajectory from an Earth-Moon L_1 Lyapunov orbit to a Sun-Earth L_2 Lyapunov orbit. To support preliminary exploration of the solution space, motion primitives for natural trajectories are independently constructed to summarize arcs along stable and unstable manifolds of L_1 and L_2 Lyapunov orbits in each of the Earth-Moon and Sun-Earth circular restricted three-body problems (CR3BP). The sequential composability of each pair of primitives is then assessed to construct a motion primitive graph. In this graph, primitives that are closely located within the configuration space are connected in two cases: if they are generated in the same CR3BP, or if a primitive from the Earth-Moon CR3BP passes close to a primitive from the Sun-Earth CR3BP at a sufficient distance from the Earth at any epoch. This graph is then searched to generate a sequence of primitives, from both dynamical models, that predicts the existence of a nearby continuous trajectory with impulsive maneuvers. Furthermore, distinct motion primitive sequences are used to generate geometrically distinct initial guesses. This approach is demonstrated by generating geometrically distinct initial guesses for planar transfers, assuming the Earth-Moon and Sun-Earth orbit planes coincide and the initial epoch is unconstrained.

BACKGROUND

Circular Restricted Three-Body Problem

The motion of a spacecraft in a three-body system is approximated using the CR3BP. This dynamical model assumes that two primary bodies gravitationally interact with a spacecraft [14]. The gravity field of each primary body, B_1 and B_2, is modeled as spherically symmetric, with constant masses [14]. However, the spacecraft is assumed to possess a negligibly small mass in comparison [14]. To support the construction of an autonomous dynamical model, the paths followed by the two primaries are assumed to be circular [14].

The CR3BP is often formulated using nondimensional coordinates. Length, mass, and time quantities are normalized to produce a distance between the two primaries, total system mass, and primary system mean motion all equal to unity [14]. In the Earth-Moon CR3BP, length and time quantities are normalized by $l^* = 384,400$ km and $t^* \approx 3.751903 \times 10^5$ sec, respectively [15]. However, in the Sun-Earth CR3BP, $l^* = 1.495979 \times 10^8$ km and $t^* = 5.022635 \times 10^6$ sec [16].

A B_1-B_2 rotating frame is defined using the locations of the two primary bodies. The origin is selected as their barycenter whereas the axes $\hat{x}\hat{y}\hat{z}$ are defined as follows [14]: $\hat{x}$ is directed from the center of the larger primary to the center of the smaller primary; $\hat{z}$ is aligned with the orbital angular momentum vector of the primaries; and $\hat{y}$ completes the right-handed, orthogonal triad. With these definitions, the nondimensional state vector of the spacecraft is defined in the rotating frame as $[\boldsymbol{r}^T, \boldsymbol{v}^T]^T$ where $\boldsymbol{r} = [x, y, z]^T$ and $\boldsymbol{v} = [\dot{x}, \dot{y}, \dot{z}]^T$; the dot notation indicates a time derivative with respect to an observer in the rotating frame.

The orientation of the rotating frame is often described relative to a general inertial frame. The axes of the inertial frame are labeled as $\hat{X}\hat{Y}\hat{Z}$. In addition, $\hat{Z} = \hat{z}$ whereas the angle between each of the $\hat{x}$ and $\hat{X}$ axes and the $\hat{y}$ and $\hat{Y}$ axes is equal to $\theta = nt$ where $n = 1$ is the nondimensional mean motion of the primary system and t is nondimensional time. The origin of the inertial frame may be selected as desired, e.g., at the system barycenter or one of the primaries. With these definitions, the nondimensional state vector of the spacecraft is defined in the inertial frame as $[\boldsymbol{R}^T, \boldsymbol{V}^T]^T$ where $\boldsymbol{R} = [X, Y, Z]^T$ and $\boldsymbol{V} = [X', Y', Z']^T$; the prime notation indicates a time derivative with respect to an observer in the inertial frame.

A state vector can be transformed between the rotating and inertial frames. The rotation matrices from the inertial frame to the rotating frame, i.e., $[^R\boldsymbol{C}^I]$, and vice versa, i.e., $[^I\boldsymbol{C}^R]$, equal

$$[^R\boldsymbol{C}^I] = \begin{bmatrix} \cos(\theta) & \sin(\theta) & 0 \\ -\sin(\theta) & \cos(\theta) & 0 \\ 0 & 0 & 1 \end{bmatrix} \qquad [^I\boldsymbol{C}^R] = \begin{bmatrix} \cos(\theta) & -\sin(\theta) & 0 \\ \sin(\theta) & \cos(\theta) & 0 \\ 0 & 0 & 1 \end{bmatrix} \tag{1}$$

where the I and R superscripts indicate the inertial and rotating frames, respectively [17]. The time derivatives of these rotation matrices are calculated as

$$[^R\dot{\boldsymbol{C}}^I] = \dot{\theta} \begin{bmatrix} -\sin(\theta) & \cos(\theta) & 0 \\ -\cos(\theta) & -\sin(\theta) & 0 \\ 0 & 0 & 0 \end{bmatrix} \qquad [^I\dot{\boldsymbol{C}}^R] = \dot{\theta} \begin{bmatrix} -\sin(\theta) & -\cos(\theta) & 0 \\ \cos(\theta) & -\sin(\theta) & 0 \\ 0 & 0 & 0 \end{bmatrix} \tag{2}$$

Then, the position and velocity vectors are transformed from the rotating frame to the inertial frame, without a change of origin, as [17]

$$\boldsymbol{R} = [^I\dot{\boldsymbol{C}}^R]\boldsymbol{r} \qquad \boldsymbol{V} = [^I\boldsymbol{C}^R]\boldsymbol{v} + [^I\dot{\boldsymbol{C}}^R]\boldsymbol{r} \tag{3}$$

When shifting the origin of the inertial frame to a primary body, as opposed to the system barycenter, a translation is applied to only $\boldsymbol{r}$ prior to this transformation [17].

The equations of motion for the CR3BP are written in nondimensional form in the rotating frame. These second-order differential equations are equal to

$$\ddot{x} - 2\dot{y} = \frac{\partial U^*}{\partial x}, \qquad \ddot{y} + 2\dot{x} = \frac{\partial U^*}{\partial y}, \qquad \ddot{z} = \frac{\partial U^*}{\partial z} \tag{4}$$

where the pseudopotential function is defined as

$$U^* = \frac{x^2 + y^2}{2} + \frac{1 - \mu}{\rho_1} + \frac{\mu}{\rho_2} \tag{5}$$

and $\rho_1 = \sqrt{(x + \mu)^2 + y^2 + z^2}$ whereas $\rho_2 = \sqrt{(x - 1 + \mu)^2 + y^2 + z^2}$ [14]. Furthermore, μ is the mass ratio, equal to $1.215058535056245 \times 10^{-2}$ in the Earth-Moon CR3BP and $3.003480594542193 \times 10^{-6}$ in the Sun-Earth CR3BP [16]. An integral of motion exists in the rotating frame and is equal to $C_J = 2U^* - \dot{x}^2 - \dot{y}^2 - \dot{z}^2$ [14]. This quantity is labeled the Jacobi constant.

Patched Circular Restricted Three-Body Problems

The patched circular restricted three-body problem offers a low-fidelity approximation of the dynamical environment when three primary bodies exert a substantial gravitational force on the spacecraft. This dynamical model has been used to design initial guesses for transfers in the Earth-Moon-Sun system by Koon, Lo, Marsden, and Ross [17] as well as Howell et al. [5]. Two CR3BPs are defined, with a common primary or barycenter of two primaries, to govern the dynamics in distinct regions. In this paper, the Earth-Moon and Sun-Earth CR3BP are employed, with the Earth serving as the larger primary in the Earth-Moon CR3BP and the smaller primary in the Sun-Earth CR3BP. Furthermore, for this proof of concept, the Earth-Moon and Sun-Earth planes are assumed to be coplanar due to the approximately 5° average angle between these planes; however, future work will eliminate this assumption. Threshold distances from the Earth are used to define which CR3BP governs the motion of the spacecraft at any instant of time.

To study the connectivity between trajectories generated in each of the Earth-Moon and Sun-Earth CR3BP, a spacecraft state vector must be transformed between distinct rotating frames and normalization schemes. Specifically, the nondimensional position and velocity vectors of the spacecraft in the Earth-Moon rotating frame, labeled as $\boldsymbol{r}_{EMB,sc}^{EM}$ and $\boldsymbol{v}_{EMB,sc}^{EM}$, are transformed to the Sun-Earth rotating frame and labeled as $\boldsymbol{r}_{SEB,sc}^{SE}$ and $\boldsymbol{v}_{SEB,sc}^{SE}$. In these vector labels, the superscripts 'EM' and 'SE' indicate the two primaries used to define the rotating frame and normalization scheme: 'E' is the Earth, 'M' is the Moon, and 'S' is the Sun. The subscripts, however, identify the basepoint and target of the vector: 'EMB' is the Earth-Moon barycenter, 'SEB' is the Sun-Earth barycenter, and 'sc' is the spacecraft. At a given epoch t, this transformation consists of the following steps, consistent with the approach presented by Koon, Lo, Marsden, and Ross [17]:

1. Translate $\boldsymbol{r}_{EMB,sc}^{EM}$ from using an origin at the barycenter of the Earth-Moon system to the Earth by adding μ to the x-component, producing $\boldsymbol{r}_{E,sc}^{EM}$. The velocity vectors are unchanged, i.e., $\boldsymbol{v}_{E,sc}^{EM} = \boldsymbol{v}_{EMB,sc}^{EM}$ as the location of the Earth is constant in the rotating frame.
2. Transform $\boldsymbol{r}_{E,sc}^{EM}$ and $\boldsymbol{v}_{E,sc}^{EM}$ from the Earth-Moon rotating frame to the inertial frame centered at the Earth using Equation 3 to produce $\boldsymbol{R}_{E,sc}^{EM}$ and $\boldsymbol{V}_{E,sc}^{EM}$.
3. Dimensionalize the position and velocity vectors in the inertial frame as well as the time using the characteristic quantities from the Earth-Moon CR3BP.
4. Nondimensionalize the position and velocity vectors in the inertial frame as well as the time using the characteristic quantities from the Sun-Earth CR3BP.
5. Transform $\boldsymbol{R}_{E,sc}^{SE}$ and $\boldsymbol{V}_{E,sc}^{SE}$ from the inertial frame centered at the Earth to the Sun-Earth rotating frame by using $[{}^{R}\boldsymbol{C}^{I}]$ and $[{}^{R}\dot{\boldsymbol{C}}^{I}]$ to produce $\boldsymbol{r}_{E,sc}^{SE}$ and $\boldsymbol{v}_{E,sc}^{SE}$.
6. Translate the position vector from using an origin at the Earth to the barycenter of the Sun-Earth system, by subtracting $1-\mu$ from the x-component to produce $\boldsymbol{r}_{SEB,sc}^{SE}$ and $\boldsymbol{v}_{SEB,sc}^{SE}$.

This transformation is influenced by the relative angle between the $\hat{x}$ axes in each of the Earth-Moon and Sun-Earth rotating frames, which is periodic over an interval labeled the synodic period and equal to 29.487 days when calculated using the characteristic quantities in this paper.

Curvature

Differential geometry is useful in studying curved paths, such as the solutions to a nonlinear, continuous time-system [18]. A trajectory that is generated from a specified initial state vector over

a time interval $t \in [t_0, t_f]$ traverses a distance equal to the arclength s that is calculated as [18]

$$s = \int_{t_0}^{t_f} ds = \int_{t_0}^{t_f} \sqrt{\dot{x}^2 + \dot{y}^2 + \dot{z}^2} dt \tag{6}$$

Furthermore, the curvature $\kappa(t)$ at a single state along the trajectory captures the deviation from a straight line in the osculating plane [19]. The unsigned curvature is calculated as

$$\kappa(t) = \frac{||\dot{\boldsymbol{r}}(t) \times \ddot{\boldsymbol{r}}(t)||}{||\dot{\boldsymbol{r}}(t)||^3} \tag{7}$$

where $\dot{\boldsymbol{r}} = \boldsymbol{v}$ is the velocity vector and $\ddot{\boldsymbol{r}} = [\ddot{x}, \ddot{y}, \ddot{z}]^T$ is the acceleration vector [19]. This expression possesses a singularity when the speed equals zero.

Density-Based Clustering

Clustering algorithms focus on discovering groupings formed by members of a dataset in a specified feature vector space [20]. Of the various approaches in the literature, density-based clustering algorithms construct clusters as members of the dataset that exist in regions of sufficiently high density [20]. The current procedure for extracting motion primitives from trajectories generated in the CR3BP, as presented by Gillespie, Miceli, and Bosanac, relies on the use of the following two density-based clustering algorithms [13]: Density-Based Spatial Clustering of Applications with Noise (DBSCAN), developed by Ester et al. [21]; and Hierarchical Density-Based Spatial Clustering of Applications with Noise (HDBSCAN), developed by Campello, Moulavi, and Sander [22].

DBSCAN discovers clusters as members that exist in high-density local neighborhoods of other members. This clustering algorithm relies on the definition of an m_{pts}-neighborhood as the local neighborhood of a current member that encompasses m_{pts} members in the selected feature vector space [21]. A core point is a member of a dataset with an m_{pts}-neighborhood that possesses a radius below a specified value ϵ. A border point lies in the m_{pts}-neighborhood of a core point but its own m_{pts}-neighborhood possesses a radius that is larger than ϵ. A noise point does not exist in the m_{pts}-neighborhood of any core points. Using these definitions, a cluster is formed by 1) core points that lie within the ϵ-sized neighborhood of other core points and 2) their associated border points [21]. Thus, DBSCAN uniquely assigns each member to either a specific cluster or as noise. This algorithm is implemented using the *dbscan* function in MATLAB [23]. A modification of DBSCAN, labeled spatio-temporal DBSCAN (ST-DBSCAN), supports clustering using information from two independent feature vector spaces [24]. In this algorithm, the definition of a core point is modified to require at least m_{pts} neighbors within a radius of ϵ_1 in the first feature vector space and at least m_{pts} neighbors within a radius of ϵ_2 in the second feature vector space [24].

HDBSCAN extends DBSCAN by removing the dependence on a specified value of ϵ. To achieve this goal, the core distance of each member of the dataset is defined as the radius of its m_{pts}-neighborhood. This information is used to calculate a mutual reachability distance between each pair of points that further separates members that exist in low-density regions. This quantity is defined between the ith and jth members of the dataset as

$$d_{reach}(\boldsymbol{f}_i, \boldsymbol{f}_j) = \max(d_{core}(\boldsymbol{f}_i), d_{core}(\boldsymbol{f}_j), d(\boldsymbol{f}_i, \boldsymbol{f}_j)) \tag{8}$$

where $d(\boldsymbol{f}_i, \boldsymbol{f}_j)$ is the distance between their feature vectors, calculated using a specified distance measure [22]. HDBSCAN uses these distances to define the edge weights of a graph where each

node corresponds to a member of the dataset [22]. A minimum spanning tree of this graph is then used to generate a hierarchy of all possible clustering results as a function of the mutual reachability distance. Clusters composed of at least $m_{minclust}$ members are selected from this hierarchy by locating groupings that maximize the stability of the result, assessed using an excess of mass definition [22]. Modifications to this cluster selection process include applying a minimum threshold ϵ_{merge} to the splitting of members into multiple clusters, as presented by Malzer and Baum [25]. Through this procedure, HDBSCAN uniquely assigns each member to either a specific cluster or as noise. Due to the use of a cluster hierarchy, irregularly shaped clusters can be extracted with distinct densities. This algorithm is implemented using the *hdbscan* library in Python [26].

TECHNICAL APPROACH

A motion primitive approach is used to generate initial guesses for planar trajectories in the patched Earth-Moon and Sun-Earth CR3BP, assuming no constraints on the initial epoch. The most recent version of the primitive extraction process, presented by Gillespie, Miceli, and Bosanac [13], is used to form a motion primitive library. These primitives summarize arcs along the hyperbolic invariant manifolds of selected L_1 and L_2 Lyapunov orbits in each of the Earth-Moon and Sun-Earth CR3BP. Then, the updated version of this primitive-based trajectory design framework, developed by Miceli and Bosanac [12], is leveraged as a foundation. Minor modifications are presented in this paper to 1) accommodate the use of primitives generated in two distinct CR3BPs, 2) implement a time-dependent assessment of their sequential composability, and 3) reduce the computational complexity of generating primitive sequences by using a hierarchical graph search.

Step 1: Generate Motion Primitive Library

Motion primitives are used to summarize arcs from stable and unstable manifolds of selected periodic orbits [13]. First, each periodic orbit is discretized into 500 states, equally spaced in arclength along the periodic orbit. Then, these states are perturbed along the planar stable and unstable modes of the periodic orbit, calculated from the monodromy matrix [17]. Each state that lies in the stable or unstable eigenspace is then propagated backward or forward in time, respectively for a duration that is equal to $\Delta t_{prop} = \Delta t_{pertdoub} + \Delta t_{des}$ [13]. In this expression, $\Delta t_{pertdoub}$ is the perturbation doubling time [27] whereas Δt_{des} is a specified, desired duration; Δt_{des} is selected as 3 months in the Earth-Moon system and 12 months in the Sun-Earth system. However, propagation terminates early if the spacecraft impacts a spherical approximation of the Sun, Earth, or Moon; their radii are equal to $695,700$ km, $6,378.137$ km, and $1,738$ km, respectively [28].

Arcs that are summarized using motion primitives are sampled from the hyperbolic invariant manifolds in a geometry-based manner [13]. As each trajectory is generated to lie in the stable or unstable manifold, the maxima in curvature are located [13]. These states correspond to geometrically meaningful locations along a trajectory, where the shape is rapidly changing. For trajectories that possess at least three curvature maxima, each arc begins at either a maximum in curvature or the initial condition [13]. Then, the arc is defined to span four additional maxima in curvature [13]. However, if the trajectory impacts any of the celestial bodies, the trajectory ends at the termination condition. If a trajectory possesses fewer than three curvature maxima, the window used to define the arc is shortened accordingly. Through this approach, every arc begins at a consistently defined location and overlaps with the previous arc, if one exists.

Each continuous arc is discretized in a geometry-based manner to produce a sequence of states [13]. First, the arc is coarsely sampled at the initial state, intermediate maxima in curvature, and the

final state, producing up to five samples. Between subsequent coarse samples, two additional samples are equally distributed in the arclength [13]. Accordingly, a trajectory with three intermediate maxima between the initial and final states is sampled using 13 states.

The sampled states are used to construct two feature vectors that capture the geometry of the trajectory in the rotating frame defined by the two primaries in the associated CR3BP, i.e., a trajectory generated in the Earth-Moon CR3BP is described using state information in the Earth-Moon rotating frame [29]. First, a shape-based feature vector $\boldsymbol{f}_s$ is defined as

$$\boldsymbol{f}_s = [\hat{\boldsymbol{v}}_1, \hat{\boldsymbol{v}}_2, ..., \hat{\boldsymbol{v}}_n]^T \tag{9}$$

where n is the number of sampled states and $\hat{\boldsymbol{v}}_i$ is the velocity unit vector at the ith sample in the rotating frame. In addition, a position-based feature vector $\boldsymbol{f}_p$ is defined using the position vectors in the rotating frame at each of the samples as

$$\boldsymbol{f}_p = [\boldsymbol{r}_1, \boldsymbol{r}_2, ..., \boldsymbol{r}_n]^T \tag{10}$$

Each feature vector is $3n$-dimensional.

Arcs extracted from the same stable or unstable half-manifold and sampled using the same number of states are coarsely clustered in the shape-based feature vector space, calculated over their entire duration, using HDBSCAN [13, 29]. At this step, $m_{pts} = 4$, $m_{minclust} = 5$, and $\epsilon_{merge} = 2\sin(5^\circ/2)$ [29]. The values of these governing parameters prioritize discovering localized variations and, therefore, lead to the large number of primitives used in this paper. Repeating this process for trajectories described by a distinct number of sampled states produces a set of coarse clusters $\mathcal{C}$ and noise. Arcs that are labeled as noise are post-processed and assigned to their nearest cluster if they lie in the ϵ-neighborhood of any of the cluster's members, where ϵ is the maximum radius of the m_{pts}-neighborhood of all core points in the cluster.

Arcs in each coarse group are input to a cluster refinement process developed by Bosanac [13, 29]. For each coarse group, the ith sampled state along each arc is used to calculate $\boldsymbol{f}_s$ and $\boldsymbol{f}_p$. DBSCAN is used to cluster the sampled states in each three-dimensional feature vector space, producing two clustering results. At this step, $m_{pts} = 4$ and $\epsilon = (m_{pts} + 1)\max(\max(e_{med}, e_{maxk}), \epsilon_{thresh})$, where e_{med} is the median distance from each member to its nearest neighbor, e_{maxk} is the $m_{minclust}$-largest distance from each member to its nearest neighbor and ϵ_{thresh} is a specified threshold; in $\boldsymbol{f}_s$, $\epsilon_{threshold} = 2\sin(5^\circ/2)$ whereas in $\boldsymbol{f}_p$, $\epsilon_{threshold} = 10^{-3}$ in the Earth-Moon system and $\epsilon_{threshold} = 10^{-4}$ in the Sun-Earth system. This process is repeated across all n samples to produce $2n$ clustering results. Any trajectories that are consistently clustered together, lie within density-connected neighborhoods in each clustering result, and possess at least $m_{minclust} = 5$ members form a refined cluster. The result is a set of clusters $\mathcal{R}$ and noise.

Each cluster is used to generate a motion primitive and its region of existence [13, 30]. The motion primitive is extracted as the medoid of the cluster in the position-based feature vector space, equal to the trajectory that follows the most similar path in the configuration space to all other trajectories. The region of existence is then the volume of the phase space spanned by all members of the cluster. Similar to the approach used by Smith and Bosanac [9] as well as Miceli and Bosanac [12], this region of existence is approximated using up to 40 trajectories that are equally distributed across the associated cluster. If a global cluster is composed of more than 40 members, a subset of 20 representative trajectories are identified by applying k-medoids clustering [31] in the position-based feature vector space of the entire trajectory using MATLAB's built-in function [23].

The clusters that are localized to each half-manifold are aggregated to produce a smaller set of global clusters, following an approach developed by Bosanac [29]. First, the motion primitive of each cluster is compared to the primitives of all other clusters that are generated to approach or depart the same periodic orbit or a neighboring periodic orbit. Then, the nearest neighboring representatives in each of the position and velocity feature vector spaces are identified. Each pair of local clusters is then input to the cluster refinement process. If any members are grouped together, the local clusters are merged. Each global cluster contains one or more merged local clusters. Upon merging, the motion primitive and region of existence are updated.

This procedure is used to generate motion primitives that summarize arcs from the stable and unstable manifolds of selected L_1 and L_2 Lyapunov orbits in the Earth-Moon and Sun-Earth CR3BP. Selected motion primitives, generated in the Earth-Moon CR3BP and Sun-Earth CR3BP are plotted in Figures 1 and 2, respectively, to summarize groups of geometrically similar arcs that approach or depart a) an L_1 Lyapunov orbit or b) an L_2 Lyapunov orbit. In these figures, the motion primitive is depicted with a thick blue curve whereas representative members of each cluster are plotted with thin blue curves. The initial state along each trajectory is indicated by a blue circle marker to supply direction of motion information. Finally, the primaries are depicted with gray circle markers; when the trajectory remains near a primary, the radius of the circle is equal to the radius of the body. In addition, L_1 and L_2 are plotted using gray diamonds. Within each subfigure, the motion primitive summarizes a set of geometrically similar trajectories. Furthermore, distinct motion primitives capture distinct geometries. For each of these four cases, the selected orbits as well as the number of clusters and assigned arcs are summarized in Table 2. Note the large number of primitives in this library is primarily due to 1) the use of small hyperparameters that prioritize discovering localized variations and 2) the large steps between the periodic orbits along each family that are used to generate arcs along stable and unstable manifolds.

Step 2: Identify Sequentially Composable Primitives

Sequencing motion primitives to form more complex paths requires identifying pairs of sequentially composable primitives. Using the procedure presented by Miceli and Bosanac [12] as a foundation, two primitives are sequentially composable if coarse approximations of their regions of

	Earth-Moon L_1 Lyapunov	Earth-Moon L_2 Lyapunov	Sun-Earth L_1 Lyapunov	Sun-Earth L_2 Lyapunov
C_J	[3.003998, 3.188089]	[3.006767, 3.172112]	[3.0007867, 3.0008907]	[3.0007891, 3.0008867]
Period (days)	[11.692, 18.480]	[14.649, 19.203]	[175.067, 179.701]	[177.562, 181.730]
Number of clustered trajectories	70,836	24,945	5,999	5,345
Number of motion primitives	5,452	3,482	628	607

Table 1. Summary of motion primitives used to summarize arcs that approach or depart selected libration point orbits in the Earth-Moon or Sun-Earth CR3BP.

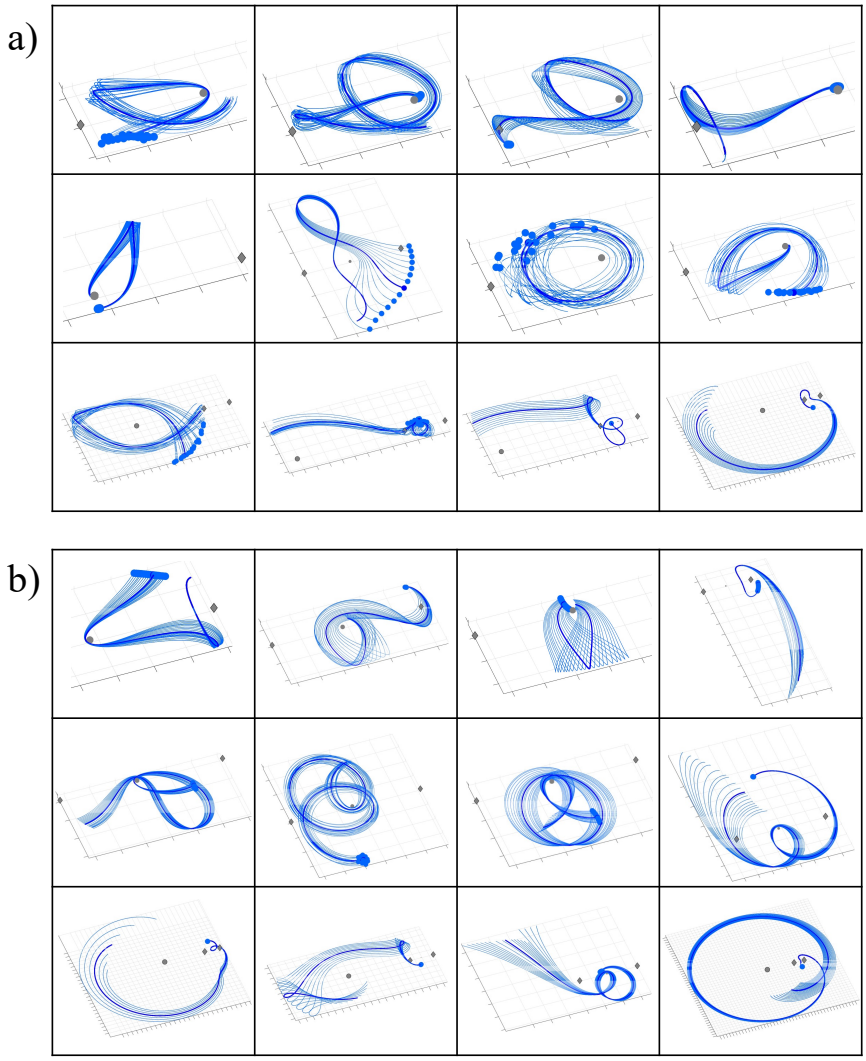

Figure 1. Selected motion primitives generated in the Earth-Moon CR3BP to approach or depart a) an L_1 Lyapunov orbit or b) an L_2 Lyapunov orbit.

existence overlap in the configuration space. The change in velocity at these overlaps is then used to estimate the "cost" of sequencing these two primitives; a similar "cost" was also used by Howell et al. when identifying intersections between manifolds using cell decompositions [5].

Following the approach presented by Miceli and Bosanac [12], each region of existence is represented by its representative trajectories and discretized into segments. Specifically, the ith segment is bound by the ith and $(i+1)$th geometry-based samples used to evaluate the feature vectors in Step 1. As an example, Figure 3a) displays a region of existence of one motion primitive P_1 from the Earth-Moon CR3BP discretized into twelve segments. Each segment is uniquely colored from cyan near the initial conditions (blue markers) to magenta at the end of the region of existence.

The region of existence associated with each primitive is coarsely approximated as a collection of circular neighborhoods around each sampled state in the configuration space, following the approach presented by Miceli and Bosanac, with minor modifications [12]. The representative tra-

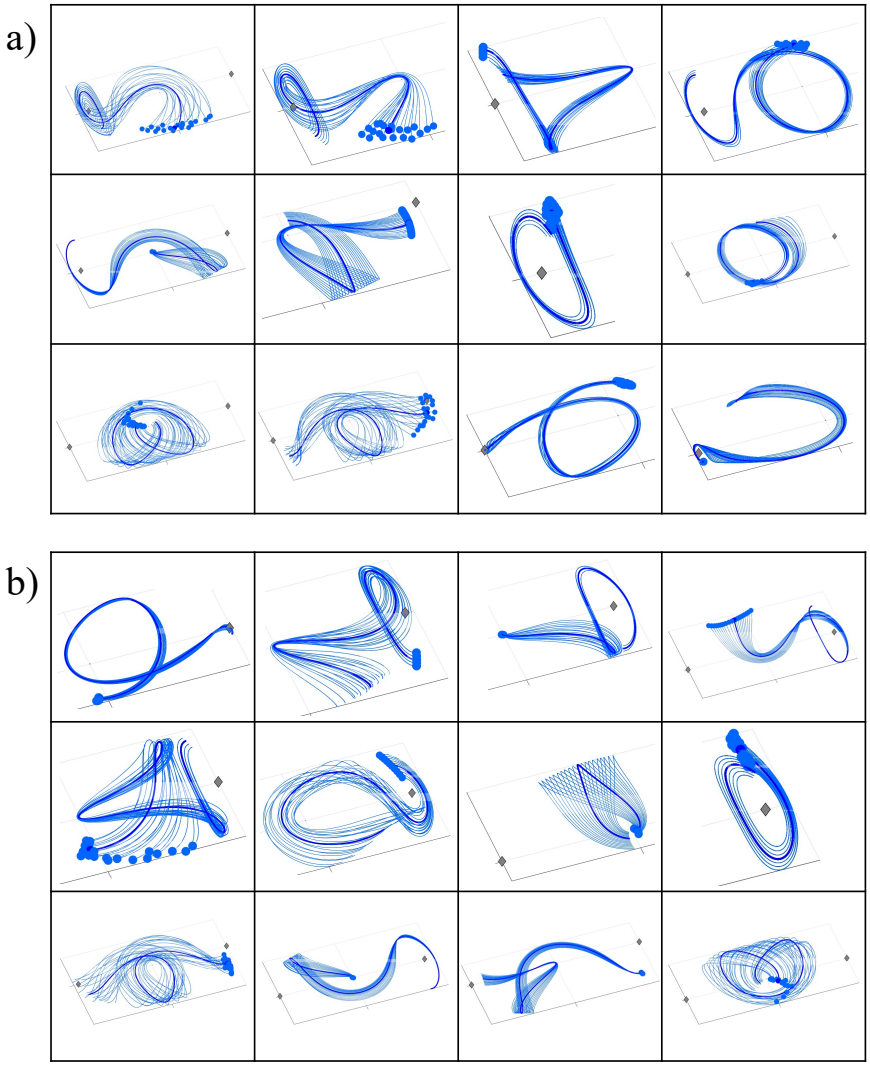

Figure 2. Selected motion primitives generated in the Sun-Earth CR3BP to approach or depart a) an L_1 Lyapunov orbit or b) an L_2 Lyapunov orbit.

jectories that span the global cluster associated with a primitive are further discretized to place up to four additional samples that are equally spaced in arclength along each segment, along with the initial state. Then, neighborhoods are constructed around each sampled state in the configuration space. For the kth sampled state within the ith segment of any trajectory in the cluster, the neighborhood radius in the configuration space is approximated as the maximum of 1) the mean distance to the 2nd-nearest neighboring position vector along any other trajectories or 2) a predefined threshold, defined as 5×10^{-3} in the Earth-Moon CR3BP or 5×10^{-4} in the Sun-Earth CR3BP. This process is repeated for all segments, coarsely approximating each region of existence via sets of circles.

To determine if two motion primitives that are generated in the same dynamical model are sequentially composable, overlapping segments of their regions of existence are identified [12]. If the coarse approximations of the regions of existence of primitives 1 and 2 overlap in the configuration space at their ith and kth segments, respectively, with a change in the velocity direction that is

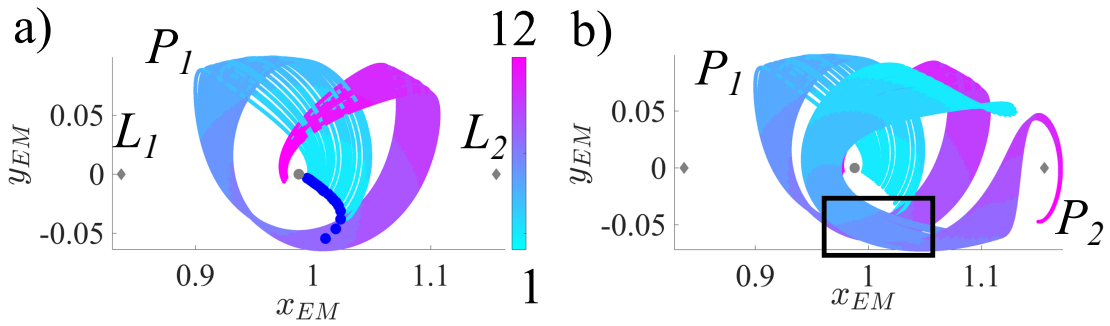

Figure 3. a) Region of existence of a motion primitive represented by up to 12 segments, colored from cyan to magenta. b) Two primitives that are sequentially composable; an example of overlapping segments is bound by the black rectangle.

less than $45°$, they are considered sequentially composable [12]. The "cost" of transitioning from primitive 1 to primitive 2 at the overlapping segments is then defined using the velocity difference to produce the following scalar quantity:

$$w_{1,i,2,k} = \min(||\boldsymbol{v}_{1,l,i} - \boldsymbol{v}_{2,m,k}||) \tag{11}$$

where the subscripts in variables such as $\boldsymbol{v}_{1,l,i}$ indicate that the velocity vector is located along a state within segment i of trajectory l within the region of existence of primitive 1. Furthermore, trajectories l and m are selected from each region of existence to minimize the velocity difference. These overlaps are identified and characterized in the rotating frame defined using the same primary bodies as the CR3BP used to generate the primitives, e.g., for primitives summarizing arcs from the Earth-Moon CR3BP, sequential composability is assessed in the Earth-Moon rotating frame.

An example of two sequentially composable primitives appears in Figure 3b). The regions of existence of primitives P_1 and P_2 are colored by their segments, from cyan to magenta, with multiple overlapping segments. As an example, segment 7 from primitive 1 overlaps with segment 5 of the region of existence of primitive 2. Accordingly, $w_{1,7,2,5}$ would be calculated using the minimum velocity difference along any of the states sampled from the associated segments.

To determine if two motion primitives that are generated in different dynamical models are sequentially composable, overlapping segments of their regions of existence are identified in the Sun-Earth CR3BP across an array of epochs [12]. In this case, consider primitive P_1 as summarizing as a set of geometrically similar arcs from the Earth-Moon CR3BP; an example is depicted in Figure 4a) in the Earth-Moon rotating frame. Each segment of this region of existence is transformed to the Sun-Earth rotating frame at a variety of epochs. Figure 4b) displays in solid blue the representative trajectories from P_1 transformed to the Sun-Earth rotating frame, using a single initial epoch $t_{0,1}$. These epochs are selected to span a full synodic period of the Earth-Moon-Sun system. Then, consider primitive P_2 as summarizing a set of geometrically similar arcs from the Sun-Earth CR3BP; the representative trajectories within its region of existence are colored according to their segment in Figure 4b). If any segments overlap within the configuration space in the Sun-Earth rotating frame, at any epoch with less than a $45°$ change in the velocity direction, the two primitives are sequentially composable. Then, Equation 11 is calculated for these overlapping segments, but modified to ensure that $w_{1,i,2,k}$ would reflect the minimum possible "cost" of sequentially composing the two primitives at these segments at any epoch.

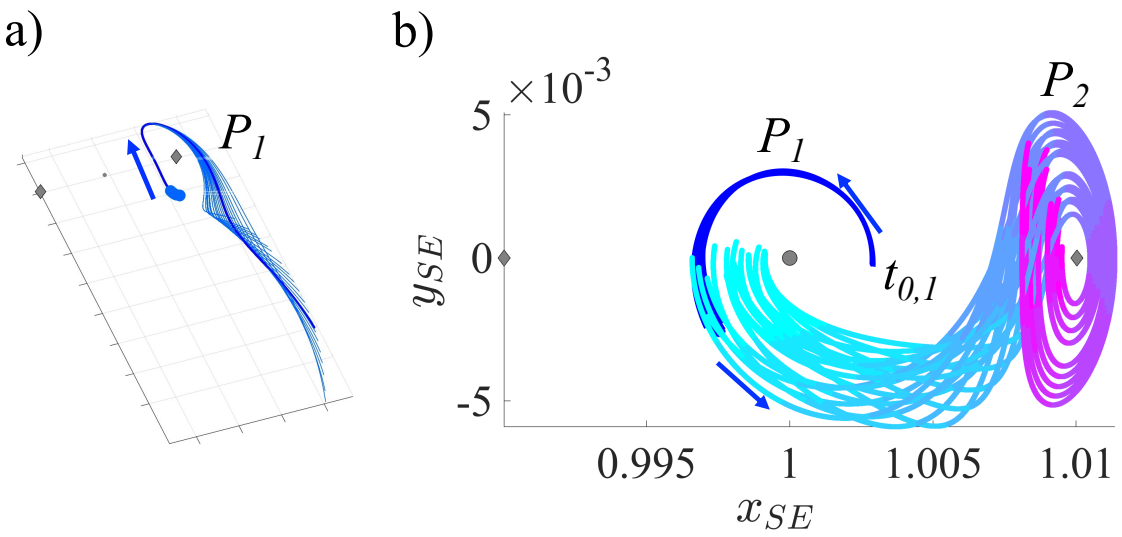

Figure 4. a) Region of existence of motion primitive 1 from the Earth-Moon CR3BP. b) Region of existence for motion primitive 1 transformed to the Sun-Earth CR3BP at a single initial epoch, plotted with motion primitive 2 from the Sun-Earth CR3BP.

Step 3: Construct Hierarchical Motion Primitive Graph

A hierarchical motion primitive graph is constructed to supply a discrete approximation of the continuous solution space that is computationally feasible to search in later steps. This hierarchical graph consists of two graphs, each formulated based on previous work. The first, high-level graph conveys the potential sequential composability of entire primitives, consistent with the approach presented by Smith and Bosanac [9]. The second, low-level graph captures the traversability of a sequence of primitives; this second graph is formulated consistent with the approach presented by Miceli and Bosanac [12]. Conceptual representations of these two graphs are depicted in Figure 5 and explained in subsequent paragraphs.

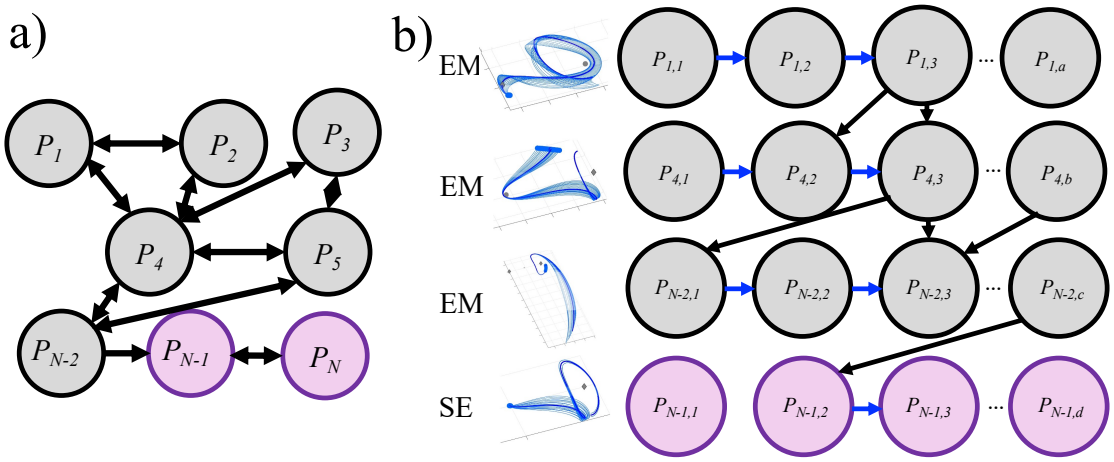

Figure 5. Structure of the hierarchical motion primitive graph: a) high-level graph and b) low-level graph.

The high-level motion primitive graph is formulated to support identifying candidate sequences of motion primitives that are composable. Accordingly, each node captures a single motion primitive from the library, as previously presented by Smith and Bosanac [9]. Directed edges are added between nodes of primitives that are sequentially composable. These edges are weighted using the minimum value of $w_{1,i,2,k}$ from Equation 11 across all possible values of i and k or, equivalently, any two overlapping segments of the regions of existence of the pair of primitives. These edge weights are also calculated in the Earth-Moon rotating frame when both primitives are generated in the Earth-Moon CR3BP. However, the edge weights are calculated in the Sun-Earth rotating frame if at least one primitive is generated in the Sun-Earth CR3BP.

The direction of the edges added between the nodes of two sequentially composable primitives depends on the dynamical model used to generate the associated arcs. If two primitives are generated in the same dynamical model, e.g., the Earth-Moon CR3BP, bidirectional edges are added as they can be traversed in any order. However, if two primitives are generated in distinct dynamical models, a unidirectional edge is only added from the primitive generated in the Earth-Moon CR3BP to the primitive generated in the Sun-Earth CR3BP. Accordingly, the trajectories are constrained to not return to the Earth-Moon system after departure in this preliminary implementation. In Figure 5a), the nodes representing primitives from the Earth-Moon CR3BP are colored gray whereas the nodes representing primitives from the Sun-Earth CR3BP are colored purple. In this conceptual figure, the only unidirectional edge is drawn from the $(N-2)$th primitive, generated in the Earth-Moon CR3BP, to the $(N-1)$th primitive, generated in the Sun-Earth CR3BP.

Similar to the formulation presented by Miceli and Bosanac [12], the low-level primitive graph is used to determine whether a primitive sequence is traversable and satisfies any path constraints. First, nodes are defined as the segments of N motion primitives from a specified sequence. In Figure 5b), a four primitive sequence is plotted on the left of the figure, labeled by the CR3BP used to generate each arc. Each primitive contributes a row of nodes to the low-level graph; gray nodes correspond to segments along primitives from the Earth-Moon CR3BP whereas purple nodes indicate the primitive is generated in the Sun-Earth CR3BP. A blue directed edge with a zero edge weight is added from the node representing the ith segment to the node of the $(i+1)$th segment along a single primitive, for $i < N_s$ where N_s is the number of segments [12]. This edge encodes natural traversal of the primitive or any geometrically similar trajectory. Then, directed edges are added between nodes from different primitives where the associated segments are sequentially composable. These edges are weighted by $w_{1,i,2,k}$ from Equation 11, evaluated using the specific values of i and k that correspond to the segments associated with the connected nodes.

Additional path constraints are applied to this low-level graph, similar to the approach presented by Miceli and Bosanac [12]. In this paper, the traversable nodes, i.e., those with edges that are connected to other nodes, are constrained to reflect the dominance of each CR3BP in distinct regions of the Sun-Earth-Moon system. A feasible segment along a primitive that is generated in the Sun-Earth CR3BP must possess at least one sampled trajectory that does not pass below a distance of 1.5 nondimensional units from the Earth when calculated using characteristic quantities from the Earth-Moon CR3BP. This constraint reflects that the Earth-Moon CR3BP is considered the dominant dynamical model below this distance, with some margin added. Similarly, a feasible segment along a primitive that is generated in the Earth-Moon CR3BP must possess at least one sampled trajectory that does not exceed a distance of 2.5 nondimensional units from the Earth when calculated using characteristic quantities from the Sun-Earth CR3BP; this value is selected using the Earth's sphere of influence. If all sampled trajectories along a segment of a region of existence

associated with a primitive violate either criterion, the node is not connected to any other nodes in the graph. In Figure 5b), the node labeled $P_{N-1,1}$, which corresponds to the first segment of the $(N-1)$th primitive violates a constraint and, therefore, has no incoming or outgoing edges. Because all motion primitives are already generated to not impact any primary bodies, no additional minimum altitude constraints are applied.

Step 4: Search Hierarchical Motion Primitive Graph

The hierarchical motion primitive graph is searched to produce paths, each composed of nodes and edges, that are transformed to primitive sequences. First, Dijkstra's algorithm is used to generate a single path through the high-level graph from a selected initial primitive to a desired final primitive. This solution is then converted to a candidate primitive sequence. This candidate primitive sequence is used to form the low-level graph that is searched using Dijkstra's algorithm for a path from the first segment of the initial primitive to the final segment of the final primitive. If a path exists, the primitive sequence is traversable and satisfies the path constraints. The connected sequence of nodes and edges through the low-level graph identified by Dijkstra's algorithm corresponds to the segments along each primitive in the sequence. In this paper, the initial epoch is assumed to be unconstrained; this assumption substantially reduces the complexity of the search process as edges between primitives from distinct dynamical models are fixed at each iteration of the graph search. Ongoing work includes incorporating a fixed initial epoch into the graph search process.

Dijkstra's algorithm is employed to generate a sequence of nodes and edges that connect a start node to an end node in a graph. This algorithm, developed by Edsger Dijkstra [32], begins by defining a priority queue that consists of the start node with a zero cost. Then, the lowest cost entry in the priority code produces a path from the start node, n_s. The final node along this path is designated as the current node, n_i. Each previously unvisited neighboring node is identified using the edges of the graph. The cumulative cost to reach neighbor n_{i+1} is then calculated as $g(n_s, n_{i+1}) = g(n_s, n_i) + g(n_i, n_{i+1})$ where $g(n_s, n_i)$ is the current cumulative cost from the start node n_s to node n_i. This neighboring node is also marked as having been visited. The cost and the path from the start node to the neighbor n_{i+1} are then added to the priority queue. This process is repeated for all neighbors of the current node. Then, the priority queue is sorted by the value of g and the lowest cost path is selected for further exploration from its last node. This process continues until the end node is reached or the priority queue is empty. If successful, the output of this process is the path that minimizes the cumulative edge weights.

To support exploring a tradespace, k candidate primitives are generated from the high-level graph. Following the work of Bruchko and Bosanac [33] and then Miceli and Bosanac [12], Yen's algorithm is used to compute these additional candidate primitive sequences. Yen's algorithm is a k-shortest paths algorithm that relies on the use of modified subgraphs to generate suboptimal solutions [34]. Once the first path through the high-level graph has been computed via Dijkstra's algorithm, the edge between nodes n_i and n_{i+1} in the solution is removed from the graph to produce a subgraph. The portion of the path from the start node n_s to the current node n_i is labeled the spur path. Then, Dijkstra's algorithm is used to generate a path through the high-level graph from node n_i to the end node n_e. This path is concatenated to the spur path. Then, the combined path is added to a list along with its total cost. This process is repeated for all edges between subsequent nodes along the most recently computed path, removing only one edge from the graph at each iteration. The next best path from those currently identified is used to repeat the process. However, at this step, if the current node is identified as n_i, all edges that connect n_i to any subsequent

nodes along previously explored solutions with the same root path are removed from the subgraph. This entire process is repeated until k candidate primitive sequences have been generated. Then, low-level graphs are constructed and searched for each candidate primitive sequence.

Step 5: Generate Initial Guess from Primitive Sequence

The sequence of segments along motion primitives, computed in the previous step, is used to generate an initial guess for a planar transfer between an L_1 Lyapunov orbit in the Earth-Moon CR3BP to a Sun-Earth L_2 Lyapunov orbit. This process follows the formulation developed by Miceli and Bosanac [12] that relies on constructing a localized graph. The result is a set of arcs, each sampled from the region of existence of a primitive, that supplies a discontinuous initial guess for a transfer while retaining the geometry of the original primitive sequence. Although this paper does not correct or optimize these initial guesses, this step is a part of ongoing work.

The localized graph defines the nodes as the traversed segments of the representative trajectories within the region of existence of each primitive in the sequence [12]. First, each of the representative trajectories spanning the region of existence of a primitive is segmented using the same procedure as described in Step 2. However, at this step, the ith segment of each trajectory between the ith and $(i+1)$th sampled states contributes a node to the graph.

Edges are added between the nodes of the localized graph in a manner that reflects the primitive sequence. First, directed, zero-weight edges are added between sequential segments along the same trajectory. Then, edges are added from the end of the last traversed segment of each trajectory associated with one primitive to the start of the traversed segment of every trajectory associated with the subsequent primitive, if their segments are sequentially composable. The edge between node i and node j is assigned the following edge weight [12]:

$$w_{i,j} = \alpha||\boldsymbol{r}_i - \boldsymbol{r}_j|| + \left(1 - \cos\left(\frac{\boldsymbol{v}_i \cdot \boldsymbol{v}_j}{||\boldsymbol{v}_i||||\boldsymbol{v}_j||}\right)\right) \tag{12}$$

where the position and velocity vectors are associated with the combination of discretely sampled states along each segment that minimize this edge weight. In this definition, the first term incentivizes reducing the position discontinuity during refinement whereas the second term includes, to a lesser extent, the change in the velocity direction through an impulsive maneuver. If the two nodes correspond to the segments of trajectories that are generated in distinct dynamical models, two modifications are employed: 1) the position and velocity vectors from the Earth-Moon CR3BP are transformed to the Sun-Earth rotating frame, and 2) the epoch that produces the lowest edge weight is used in this calculation. Finally, $\alpha = 1$ when the trajectories associated with both nodes are generated in the Earth-Moon CR3BP whereas $\alpha = 10$ when the trajectories of at least one node is generated in the Sun-Earth CR3BP. This difference in the scalar value α accounts for the distinct nondimensional length scales in the vicinity of the smaller primary in the distinct dynamical models.

The localized graph is searched using Dijsktra's algorithm to generate a sequences of nodes and edges that minimizes the cumulative edge weight. These nodes and edges supply a sequence of arcs that focus on reducing the state discontinuity while still resembling the segments along the original primitive sequences. These arcs form the initial guess for a trajectory. In this paper, both the total velocity discontinuity between arcs and the flight time are reported with each initial guess. However, this first quantity does not directly translate to the total Δv as the initial guess is discontinuous.

RESULTS

The motion primitive approach is used to generate initial guesses between selected primitives in the Earth-Moon CR3BP and Sun-Earth CR3BP. The high-level motion primitive graph is formed using all 10,169 members of the motion primitive library. Searching this graph produces 10,000 candidate primitive sequences that connect the following boundary conditions: 1) a primitive from the Earth-Moon CR3BP approaching an L_1 Lyapunov orbit at $C_J = 3.09273$, representing arrival into a staging orbit that supplies the initial condition, and 2) a primitive from the Sun-Earth CR3BP approaching an L_2 Lyapunov orbit at $C_J = 3.000799$, serving as the target condition. Each candidate primitive sequence is refined, generating 2,239 traversable sequences of primitive segments that also satisfy the path constraints.

Eight examples of geometrically distinct initial guesses between various initial and final primitives are depicted in Figures 6-7. The lefthand side of each figure depicts part of the initial guess in the Earth-Moon rotating frame, zoomed into the vicinity of the Moon, whereas the righthand side of each figure depicts part of the initial guess in the Sun-Earth rotating frame. In this rightmost subfigure, the arcs generated in the Earth-Moon CR3BP are plotted in red whereas the arcs generated in the Sun-Earth CR3BP are plotted in blue. Across all subfigures, the start of each arc is indicated by a circle with the arrows indicating direction of motion. The locations of the Earth and Moon are plotted, but not to scale. The total velocity discontinuities and flight times of these eight initial guesses are listed in Table 2, rounded to the nearest integer value.

In these eight examples, the transfers are geometrically distinct and visually appear to produce paths with relatively low position discontinuities. The transfers in Figure 6a) and b) possess a similar path in the lunar vicinity, performing one revolution around the Moon before departing through the L_2 gateway with a high energy. However, they possess a distinct phasing in the Sun-Earth system with Figure 6b) featuring nearly a complete revolution around the Earth. In contrast, Figures 6c) and d) feature paths that complete two or no full revolutions around the Moon before departing through the Earth-Moon L_2 gateway, but with a similar phasing in the Sun-Earth system. The transfers in Figures 7a) and b) exhibit substantially different geometries within the Earth-Moon system, performing a close pass of the Moon and revolving around distinct libration points at a substantially higher energy than the initial condition. Finally, Figures 7c) and d) feature transfers that depart through the L_1 gateway to temporary revolve around the Earth before returning and performing a close pass of the Moon, then revolving near a higher energy L_2 Lyapunov orbit. In Figure 7c), the revolutions around the Earth resemble a 3:1 resonant orbit.

Subfigure	6a)	6b)	6c)	6d)
Velocity discontinuity (m/s)	233	127	292	223
Flight time (days)	251	312	343	307
Subfigure	7a)	7b)	7c)	7d)
Velocity discontinuity (m/s)	133	458	982	172
Flight time (days)	275	276	323	332

Table 2. Velocity discontinuity and flight time of the initial guesses from Figures 6 and 7.

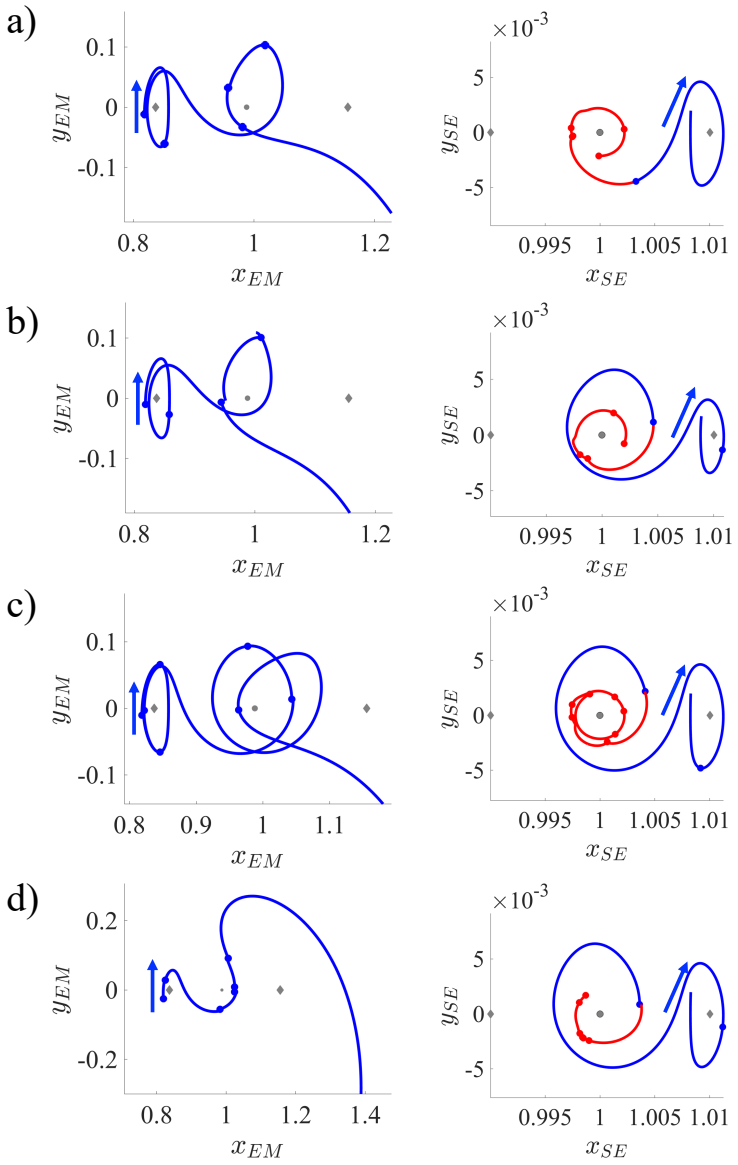

Figure 6. Examples of initial guesses for transfers from an arc approaching an Earth-Moon L_1 Lyapunov orbit to an arc approaching a Sun-Earth L_2 Lyapunov orbit.

CONCLUSIONS

This paper leveraged a motion primitive approach to generate planar initial guesses for spacecraft trajectories from an Earth-Moon L_1 Lyapunov orbit to a Sun-Earth L_2 Lyapunov orbit. This paper leveraged an approach previously developed by Miceli and Bosanac [12], with minor modifications to 1) use primitives from two different dynamical models, 2) incorporate time dependency into the assessment of sequential composability, and 3) reduce the computational complexity of searching for multiple primitive sequences. The presented examples demonstrate the capability for the motion primitive approach to generate geometrically distinct initial guesses for further corrections and optimization. This variety in the initial guesses supports automated and efficient exploration of the

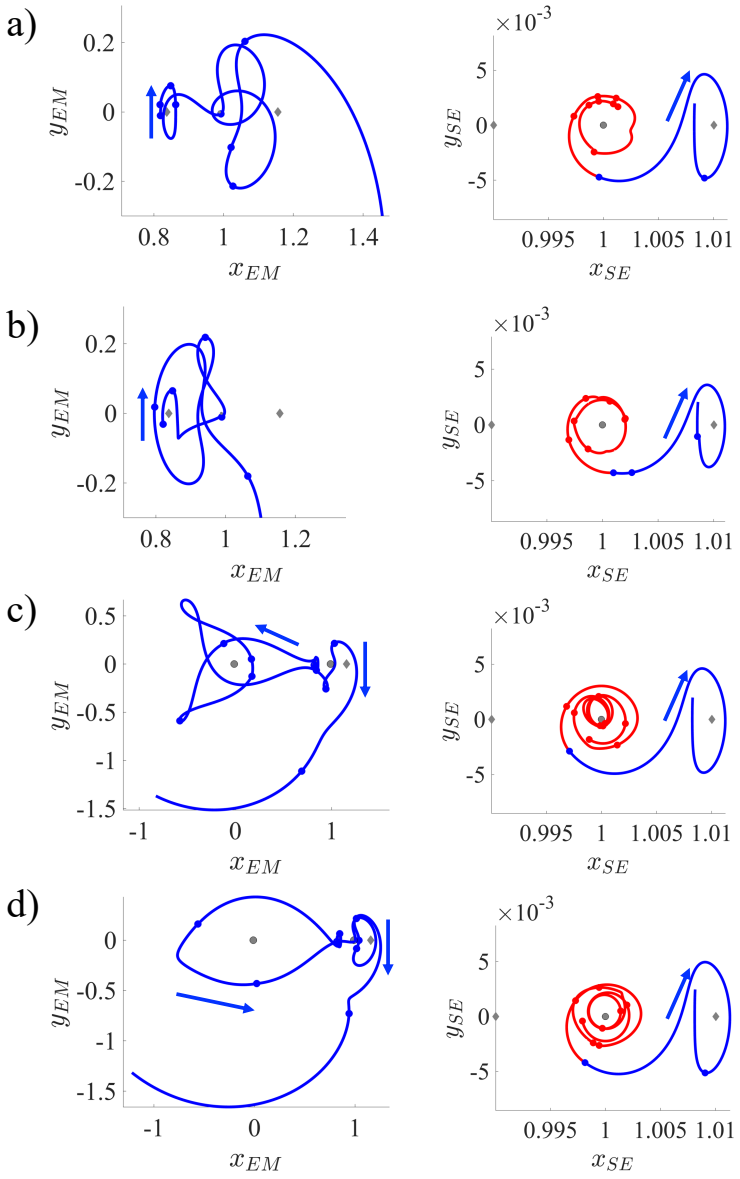

Figure 7. Examples of initial guesses for transfers from an arc approaching an Earth-Moon L_1 Lyapunov orbit to an arc approaching a Sun-Earth L_2 Lyapunov orbit.

solution space. Expanding this tradespace to encompass spatial transfers and a wider variety of initial orbits may eventually support answering key trajectory-focused questions in the development of robotic servicer capabilities.

ACKNOWLEDGMENT

Part of this paper is based upon work supported by the Air Force Office of Scientific Research under award number FA9550-23-1-0235. Any opinions, findings, and conclusions or recommendations expressed in this material are those of the authors and do not necessarily reflect the views of the United States Air Force.

REFERENCES

[1] H. Willenberg, M. Fruhwirth, and S. Potter, "Site Selection and Deployment Scenarios for Servicing of Deep-Space Observatories," in *IEEE Aerospace Conference*, 2002.

[2] C. Lillie, "On-Orbit Servicing for Future Space Observatories," in *Space 2005*, Long Beach, CA, Aug. 2005.

[3] B. Naasz, "Concepts for Servicing Habitable Worlds Observatory," in *Pioneering Sustainable Observatories, Summer 2024 Workshop Exploring Servicing Capabilities for the Habitable Worlds Observatory*, Presentation, 2024.

[4] R. Farquhar, D. Muhonen, and L. Church, "Trajectories and Orbital Maneuvers for the ISEE-3/1CE Comet Mission," in *AAS/AIAA Astrodynamics Conference*, Seattle, WA, 1984.

[5] K. Howell, M. Beckman, C. Patterson, and D. Folta, "Representations of Invariant Manifolds for Applications in Three-Body Systems," *The Journal of the Astronautical Sciences*, vol. 54, no. 1, pp. 69–93, 2006.

[6] D. Folta and C. Webster, "Transfer Trajectory Options for Servicing Sun-Earth-Moon Libration Point Missions," in *AAS/AIAA Space Flight Mechanics Meeting*, Ka'anapali, HI, 2019.

[7] J. Romero and K. Howell, "Transfers from Geosynchronous Transfer Orbits to Sun-Earth Libration Point Trajectories," *The Journal of the Astronautical Sciences*, vol. 69, pp. 251–283, 2022.

[8] A. Pascarella, R. Bommena, S. Eggl, and R. Woollands, "Mission Design for Space Telescope Servicing at Sun-Earth L2," *Acta Astronautica*, pp. 397–414, 2024.

[9] T. Smith and N. Bosanac, "'Motion Primitive Approach to Spacecraft Trajectory Design in a Multi-Body System," *The Journal of the Astronautical Sciences*, vol. 70, no. 34, 2023.

[10] A. Wolek and C. Woolsey, "Model-Based Path Planning," in *Sensing and Control for Autonomous Vehicles: Application to Land, Water and Air Vehicles*. Berlin: Springer, 2017.

[11] T. Smith and N. Bosanac, "Constructing Motion Primitive Sets to Summarize Periodic Orbit Families and Hyperbolic Invariant Manifolds in a Multi-Body Systems," *Celestial Mechanics and Dynamical Astronomy*, vol. 134, no. 7, 2022.

[12] G. Miceli and N. Bosanac, *Generating Trajectories for Neptunian System Exploration Using Motion Primitives*, Under review, 2025.

[13] G. Gillespie C. Miceli and N. Bosanac, "Summarizing Natural and Controlled Motion in Cislunar Space With Behavioral Motion Primitives," in *AAS/AIAA Space Flight Mechanics Meeting*, Kaua'i, HI, Jan. 2025.

[14] V. Szebehely, *Theory of Orbits: The Restricted Problem of Three Bodies*. London: Academic Press, 1967.

[15] NASA Jet Propulsion Laboratory Solar System Dynamics, *Horizons System*, Last Accessed: August 22, 2025, 2025.

[16] W. Folkner, J. Williams, and D. Boggs, "The Planetary and Lunar Ephemeris DE 421," *The Interplanetary Network Progress Report*, vol. 42, no. 178, 2009.

[17] W. S. Koon, M. W. Lo, J. E. Marsden, and S. D. Ross, *Dynamical Systems, the Three Body Problem and Space Mission Design*. New York: Marsden Books, 2011.

[18] K. Wardle, *Differential Geometry*. Mineola, NY: Dover Publications, Inc., 2008.

[19] N. Patrikalakis, T. Maekawa, and W. Cho, *Shape Interrogation for Computer Aided Design and Manufacturing*. 2009.

[20] J. Han and M. Kamber, *Data Mining: Concepts and Techniques, 2nd ed.* New York, NY: Proquest EBook Central: Elsevier Science and Technology, 2006, ch. 7.

[21] M. Ester, H. Kriegel, J. Sander, and X. Xu, "A Density-Based Algorithm for Discovering Clusters in Large Spatial Databases with Noise," in *Proceedings of the Second International Conference on Knowledge Discovery and Data Mining*, AAAI Press, 1996.

[22] R. Campello, D. Moulavi, and J. Sander, "Density-Based Clustering Based on Hierarchical Density Estimates," in *Advances in Knowledge Discovery and Data Mining*, J. Pei, V. Tseng, L. Cao, H. Motoda, and G. Xu, Eds., Heidelberg: Springer, Berlin, 2013.

[23] The MathWorks Inc., *MATLAB version: 9.14 (R2023a)*, Natick, Massachusetts, United States, 2023. [Online]. Available: `https://www.mathworks.com`.

[24] D. Birant and A. Kut, "ST-DBSCAN: An Algorithm for Clustering Sspatial–Temporal Data," *Data Knowl. Eng.*, vol. 60, pp. 208–221, 2007, DOI: 10.1016/j.datak.2006.01.013.

[25] C. Malzer and M. Baum, "A Hybrid Approach To Hierarchical Density-Based Cluster Selection," in *2020 IEEE International Conference on Multisensor Fusion and Integration for Intelligent Systems*, 2020, pp. 223–228.

[26] L. McInnes, J. Healy, and S. Astels, "hdbscan: Hierarchical Density Based Clustering," *Journal of Open Source Software*, vol. 2, no. 11, 2017.

[27] J. S. Parker and R. L. Anderson, *Low-Energy Lunar Trajectory Design*. Hoboken, New Jersey: John Wiley & Sons, 2014.

[28] NASA Goddard Space Flight Center, *General Mission Analysis Tool Version R2020a: Mathematical Specifications*, 2020.

[29] N. Bosanac, "Data-Driven Summary of Motion in an Ephemeris Model of Cislunar Space," in *AAS/AIAA Space Flight Mechanics Meeting*, Kaua'i, HI, Jan. 2025.

[30] N. Bosanac, "Data-Mining Approach to Poincaré Maps in Multi-Body Trajectory Design," *Journal of Guidance, Control, and Dynamics*, vol. 43, no. 6, 2020.

[31] L. Kaufman and P. Rousseeuw, "Finding Groups in Data," in John Wiley Sons, Inc., 1990, ch. Partitioning Around Medoids (Program PAM), doi:10.1002/9780470316801.ch2.

[32] E. Dijkstra, "A Note on Two Problems in Connexion with Graphs," *Numerische Mathematik*, vol. 1, pp. 269–271, 1959, doi:10.1007/BF01386390.

[33] K. Bruchko and N. Bosanac, "Rapid Trajectory Design in Multi-Body Systems Using Sampling-Based Kinodynamic Planning," *The Journal of the Astronautical Sciences*, vol. 72, no. 33, 2025.

[34] J. Yen, "Finding the k Shortest Loopless Paths in a Network," *Management Science*, vol. 17, pp. 712–716, 1971.